



HAL
open science

Super-resolution for everybody: An image processing workflow to obtain high-resolution images with a standard confocal microscope

France Lam, Damien Cladière, Cyndélia Guillaume, Katja Wassmann,
Susanne Bolte

► To cite this version:

France Lam, Damien Cladière, Cyndélia Guillaume, Katja Wassmann, Susanne Bolte. Super-resolution for everybody: An image processing workflow to obtain high-resolution images with a standard confocal microscope. *Methods*, 2016, pp.17-27. 10.1016/j.ymeth.2016.11.003 . hal-01396638

HAL Id: hal-01396638

<https://hal.sorbonne-universite.fr/hal-01396638>

Submitted on 14 Nov 2016

HAL is a multi-disciplinary open access archive for the deposit and dissemination of scientific research documents, whether they are published or not. The documents may come from teaching and research institutions in France or abroad, or from public or private research centers.

L'archive ouverte pluridisciplinaire **HAL**, est destinée au dépôt et à la diffusion de documents scientifiques de niveau recherche, publiés ou non, émanant des établissements d'enseignement et de recherche français ou étrangers, des laboratoires publics ou privés.

Title:

Super-resolution for everybody: An image processing workflow to obtain high-resolution images with a standard confocal microscope

Authors:

France Lam¹, Damien Cladière², Cyndélia Guillaume¹, Katja Wassmann², and Susanne Bolte^{1*}

¹Sorbonne Universités, UPMC Univ Paris 06, CNRS, Core Facilities - Institut de Biologie Paris Seine (IBPS), 75005 Paris,

²Sorbonne Universités, UPMC Univ Paris 06, CNRS, Laboratory of Developmental Biology - Institut de Biologie Paris Seine (IBPS), 75005 Paris, France

*Corresponding author: susanne.bolte@upmc.fr

Abstract

In the presented work we aimed at improving confocal imaging to obtain highest possible resolution in thick biological samples, such as the mouse oocyte. We therefore developed an image processing workflow that allows improving the lateral and axial resolution of a standard confocal microscope. Our workflow comprises refractive index matching, the optimization of microscope hardware parameters and image restoration by deconvolution. We compare two different deconvolution algorithms, evaluate the necessity of denoising and establish the optimal image restoration procedure. We validate our workflow by imaging sub resolution fluorescent beads and measuring the maximum lateral and axial resolution of the confocal system. Subsequently, we apply the parameters to the imaging and data restoration of fluorescently labelled meiotic spindles of mouse oocytes. We measure a resolution increase of approximately 2-fold in the lateral and 3-fold in the axial direction throughout a depth of 60 μm . This demonstrates that with our optimized workflow we reach a resolution that is comparable to 3D-SIM-imaging, but with better depth penetration for confocal images of beads and the biological sample.

Highlights

- We propose a workflow that allows obtaining 3D-SIM-like resolution with a standard confocal microscope.
- We improve the resolution of confocal imaging 2-fold in the lateral direction and 3-fold in the axial direction and up to a depth of 60 μm .
- We evaluate two different deconvolution algorithms and the effect of denoising on the deconvolution result.

- We show that with this approach, 3D-SIM-like resolution may be obtained of microtubules in the meiotic spindle of mouse oocytes.

Key words

Confocal microscopy, deconvolution, refractive index matching, 3D-SIM-like resolution improvement, meiotic spindle

1. Introduction

During the past ten years one of the most fundamental challenges in 3D imaging was to break the diffraction barrier of light in optical microscopy to attain super-resolution images [1]. These new super-resolution techniques may be based on the precise localization of fluorochromes, such as PALM/STORM, which needs high power excitation and numerous acquisitions to collect enough photons. On the other hand, non-linear fluorophore responses such as Stimulated Emission Depletion (STED) help increasing the resolution. STED is based on the selective deactivation of fluorophores by a high power depletion laser, minimising the area of illumination at the focal point, and thus enhancing the achievable resolution for a given system. Sample preparation in PALM/STORM and STED-microscopy demands for dyes with specific characteristics and fluorochrome environment, especially if multicolour labelling is needed. Another major drawback is that 3D-information is difficult to achieve and the depth penetration of these techniques is limited to a few μm for PALM/STORM and below 20 μm for STED.

3D-Structured Illumination Microscopy (3D-SIM), a technique based on illumination patterning has recently emerged as a practicable approach to circumvent the diffraction limit of light, avoiding complex sample preparation protocols. 3D-SIM requires the acquisition of at least 15 images per plane and the image contrast has to be good enough to extract high frequencies. 3D-SIM allows obtaining a spatial resolution of 100-150 nm laterally and 250-350 nm axially, thus improving resolution by a factor of approximately two compared to confocal microscopy [1, 2, 3]. This technique has enabled high resolution imaging of the cellular components such as the microtubule (MT) network in cells and organisms [4, 5]. However, standard 3D-SIM is limited to an imaging depth of 10-20 μm [6] and therefore difficult to achieve in thicker samples. The reasons for this are the inherent out-of-focus background of this wide-field approach. Furthermore, bulky samples do not allow obtaining a good fringe contrast necessary for the reconstruction of the 3D-SIM-image. Using two-photon SIM, the depth penetration limit has been broken enabling super-resolution imaging in depth beyond 45 μm [5, 7]. Yet, 3D-SIM and 2-photon SIM are methods that call for specialised equipment and expertise, and are not accessible to every biologist. PALM/STORM, STED and 3D-SIM

require image reconstruction/processing as a final step and can be applied in a restricted manner to live imaging [1]. However, even though these techniques have been democratized recently by the emergence of commercial solutions they ask for high technical expertise and specific hardware, they are time consuming and display inherently high photo-toxicity [1].

On the other hand, confocal microscopy, a valuable tool for optical sectioning of thick samples has become a standard technique accessible to every biologist. A conventional confocal microscope may reach resolutions of 200 nm laterally and 500 nm axially, if properly adjusted [8]. Furthermore, image restoration by deconvolution, a powerful computational process used to reduce out-of-focus light in 3D-fluorescent images, can be combined with confocal imaging. This combination has been proven useful to enhance image contrast, improve the signal-to-noise ratio and resolution [9, 10, 11]. However, deconvolution of confocal data is still scarcely used. This might be due to the fact that deconvolution requires expertise and a neat measurement of the impulse response of the optical system; the point spread function (PSF). When focussing deep into a biological specimen the PSF is distorted by spherical aberrations due to refractive index mismatches [12], and might then not be precise enough to perform high fidelity deconvolution. Besides, scattering is also an issue in thick and optically dense samples. To counteract the negative influence of the distorted PSF on the deconvolution results, one might use a PSF taken directly from the biological image, if the structures investigated have the appropriate shape [13]. It is also possible to compute theoretical PSF [14]. Alternatively, adaptive optics could be used to minimize the distortion of the wave front in depth of the sample [15]. Another possibility to avoid spherical aberration and thus distortion of the PSF would be refractive index matching of the sample [16]. We have recently shown that accurate refractive index matching of the sample and the mounting medium improves considerably the axial resolution and depth penetration in fixed brain tissue [17]. We furthermore showed that the fixed biological tissue has an overall refractive index that is close to that of the optical system (1.518), rendering the tissue very transparent. This minimizes scattering and the PSF measured after focussing up to 120 μm into this sample was not impaired by spherical aberration and thus distortion-free.

In the present study, we aim at applying this knowledge on the mouse oocyte, a rather bulky sample with a diameter of nearly 100 μm . Our scientific project aims at improving microtubule (MT) imaging at high resolution in the meiotic spindle. High resolution imaging of the meiotic spindle will be important to tackle outstanding questions regarding the influence of the structural organisation of the MTs network on meiotic division in the future. Microtubules of the meiotic spindle are hollow tubes of 25 nm in diameter, consisting of 13 protofilaments composed of alpha- and beta-tubulin heterodimers. These polymers are highly dynamic and stochastically switch between polymerisation and depolymerisation, a process known as dynamic instability [18]. MT dynamics and structural

organisation is tightly regulated by a plethora of MT-associated proteins (MAPs) [19]. To understand how the precise organisation of the MT network contributes to essential cellular processes such as chromosome segregation during meiosis, a detailed reconstruction and analysis of the spatial distribution of MTs as well as their length, orientation and anchoring to kinetochores in oocytes is decisive. However, conventional fluorescence microscopy of these polymers and their associated proteins in mammalian oocytes is limited by light diffraction and by the thickness of the sample. Visualizing the attachment of individual microtubule fibres on each sister kinetochore is beyond the resolution limit of classical confocal imaging.

In the present paper, we combine refractive index matching, optimisation of imaging parameters and deconvolution of confocal data. Several commercial solutions have been recently developed to improve lateral and axial resolution of confocal imaging. Leica's Hyvolution and Olympus' FV-OSR solution both use a standard confocal microscope, customized with optimized acquisition and detection system (pinhole closure and high sensitivity, low-noise detector) coupled to image restoration. A different approach is used in the Zeiss' Airyscan configuration where all photons are collected from the volume excited with concentrically arranged hexagonal detector array. Its detection area consists of 32 single detector elements, acting as very small pinholes. The signals from these detector elements are reassigned to their correct position, producing an image with increased signal-to-noise ratio and resolution.

We propose a workflow similar to the solution from Leica and Olympus, with the difference, that we adapt the mounting medium by refractive index matching with the biological sample. This matching decreases the impact of the spherical aberration and improves thus axial resolution. Our workflow allows to improve the lateral and axial resolution of the confocal microscope, gaining resolutions comparable to 3D-SIM-imaging, but with a much better depth penetration. In a first step, we characterize the resolution of our optical system by acquiring sub resolution fluorescent beads using this workflow. We then demonstrate that this optimized workflow improves considerably the resolution of biological imaging when applied to the meiotic spindle of mouse oocytes.

2. Materials and Methods

2.1 Oocyte culture and whole-mount immunofluorescence

Oocytes were obtained from ovaries of adult Swiss mice 10 to 16 weeks old (Janvier, France) and cultured in self-made M2 medium, as previously described [20]. Oocytes entering meiosis I, visible through Germinal Vesicle Breakdown (GVBD), within 60 min after harvesting were used for experiments. Before using oocytes for fixation, the zona pellucida was removed by incubation in Tyrode's solution [21].

Between 6h and 6h30 after GVBD, zona pellucida-free oocytes were placed into self-made chambers in order to manipulate them easily. Oocytes were cytospinned in chambers coated with concanavalin A (at 0.2mg/ml, from Sigma) to keep oocytes in place, for 13 min at 1400 RPM at 38°C. Cold-stable spindles were obtained by incubating the individual chambers on an ice-water bath for 4 min before fixation. Oocytes were fixed with 2 % Formaldehyde solution (Sigma-Aldrich; F1635) in BRB80 buffer with Triton TX-100 during 30min at 38°C, as described [22]. After PBS washing, oocytes were incubated overnight in a PBS-BSA 3% Triton TX-100 solution for permeabilisation and blocking unspecific antibody binding.

Antibody staining of fixed oocytes was done using the antibodies below at the indicated dilutions in PBS: Human CREST autoimmune antibody (Celon SA, HCT-0100; 1/100), and mouse monoclonal α -tubulin (DM1A) coupled to FITC (Sigma-Aldrich, F2168; 1/100). As secondary antibody CY3 anti rabbit (Jackson ImmunoResearch, 711-166-152; 1/200) was used. Antibody incubation times were at least one hour. Chromosomes were stained with 5 μ g/ml Hoechst 33342 during incubation with the secondary antibody. Oocytes were washed several times with PBS between antibody incubations and before mounting the chamber [22].

2.2 Mounting media

We used AF1 (Citifluor, UK), a commercially available mounting medium with a refractive index of 1.463 and AF1+, a modified AF1 solution harbouring a refractive index of 1.518. The refractive index increase of AF1+ solution was obtained by adding 83 % (w/w) of Methyl-Phenylsulfoxid (Sigma-Aldrich, #261696) to AF1-solution. Refractive indices were verified at 21°C using a refractometer (Mettler Toledo, Switzerland).

2.3 Preparation of Sub-resolution fluorescent beads

The experimental setup for evaluating lateral and axial resolution at the coverslip and in depth was designed as followed: fluorescent beads (PS-Speck, Lifetechnologies), of a diameter of 100 nm, and loaded with yellow-green fluorescent dye, were diluted in water (1/800 v/v). Drops of the water-

diluted sample were put on the surface of the coverslip (Menzel Glaeser #1.5, Agar scientific) or slide and air-dried. The coverslip and slide were separated by one layer of adhesive tape (Scotch®, 3M) with a nominal thickness of 60 μm and the volume filled with a drop of the respective mounting medium.

2.4 Confocal laser scanning microscopy

8-bit Images were collected using a Leica 63x oil immersion objective (HCX Plan APO CS, NA 1.4, working distance 0.14 mm) with an inverted Leica laser-scanning confocal microscope TCS SP5 II (Leica Microsystems, Heidelberg, Germany) equipped with a GaAsP hybrid detection system at a sampling rate of 40 nm in x,y- and 83 nm in z-direction unless otherwise stated. Fluorochromes were detected using laser lines 405 nm, 488 nm and 561 nm. Imaging was performed in a temperature-controlled room at 21°C. The detection pinhole aperture was adjusted to 1 Airy unit or 0.6 Airy units. Slow scanning speeds may improve the signal-to-noise ratio and the resolution of the image since more photons may be collected by pixel. The cutoff value has to be determined for every biological sample, since slower scan speed results in higher photo bleaching. We tested scan speeds of 400, 200, 100 and 50 Hz. For the given biological sample the optimal scan speed was 400 Hz. We also tested Immersion oils with refractive indexes from 1.510 to 1.520 to minimize spherical aberration (supp. figure 2). We used an immersion oil harbouring a refractive index of 1.518 for all image acquisitions.

2.5 Image acquisition of beads

Bead images were obtained as in [17] with the following modifications. GaAsP gain was set to 15% and the laser power adjusted so that the signal occupied the full dynamic range of the detector, but saturated voxels were carefully avoided. Beads were imaged starting and finishing the stack at least 5 μm below and above the bead centre. Beads were visually checked and improper stacks were discarded before determining the microscope PSF.

Beads used for resolution measurements (Fig. 1) were acquired at a sampling rate of 32 nm in x, y and 42 nm in z-direction. An average of 60 beads was taken for each measurement. Beads used for deconvolution were acquired at a sampling rate of 40 nm in x,y and 83 nm in z-direction. At least 15 beads were registered and averaged in order to increase the SNR for deconvolution.

2.6 Resolution measurement with beads

Resolution measurements were carried out as in [18] using ImageJ with the following modifications: We took the maximum intensity plane of the image stack along the x, y and z-axis resulting in 1D intensity profiles. A x,y- and z-line-profile was generated manually along a line passing through the

2D maximum. From this image, fluorescence intensity profiles were fitted to a Gaussian curve, using ImageJ's built-in curve fitting function. The full width at half maximum (FWHM) of the gaussian curve was calculated for each profile, based on the parameters retrieved from the fitting (supp. fig. 3 A).

2.7 Deconvolution and image treatment:

Confocal images of beads and biological data were deconvoluted with the Huygens 3.7 software (Scientific Volume Imaging, Hilversum, Netherlands) using a measured PSF (supp. fig. 3B). We tested the Classical Maximum Likelihood Estimation (CMLE) algorithm and the Good's (GMLE) algorithm. Signal-to-noise ratios, also called the R-parameter from 15 to 20 are recommended by the manufacturer for noisy confocal images R-values > 20 for low noise wide-field images. Since we used a confocal microscope with a low noise detector, we tested R-parameters of 26 to 34 and visually inspected the results. In images of figure 2 to 6 brightness and contrast were adjusted equally for all images after deconvolution and before 3D reconstruction and volume rendering. Image analysis was performed with ImageJ [23] and 3D-volume rendering was performed with ICY [24]. Deconvolution was performed with a measured PSF, with a quality threshold of 0.001, varying R-parameters as stated, performing 500 iterations in the optimized mode with CMLE-method and 125 iterations with the GMLE-method. Denoising was performed using the Pure Denoise Plugin [25, 26, 27] implemented in ImageJ with the cycle spin and the multiframe parameter set to maximum.

2.8 Signal to Noise Ratio calculation

To calculate the SNR, we choose a threshold with the Shanbhag mode on ImageJ (supp. figure 4). We created a mask to measure the average intensity of our structure and with the inverted thresholded image; we create a second mask to measure the average intensities of the background. We finally calculate the SNR as average intensity/average background.

3. Results and discussion

3.1 Resolution measurement using sub-resolution microspheres

We first aimed at developing a workflow, consisting of optimized sample preparation, image acquisition and deconvolution parameters to obtain the best resolution with our standard confocal microscope. We therefore investigated the lateral and axial resolution of the confocal microscope, using a high numerical aperture lens (63x, NA 1.4, oil immersion).

We determined the Point Spread Function (PSF) using two different mounting media, and varying the detection pinhole aperture. The PSF is the impulse response of the focused optical system and gives information about the lateral and axial resolution of the optical system. The PSF was measured by imaging 3D stacks of 100 nm fluorescent beads at different depths. The lateral and axial resolutions

were estimated from the full-width at half-maximum (FWHM) of the intensity profile of the PSF. We compared beads mounted in AF1 with a refractive index of 1.463 with beads mounted in AF1+, a modified AF1, harbouring a refractive index of 1.518. In the first case we introduced a mismatch of the refractive index (n_i) between the sample ($n_i=1.463$) and the glass-oil-interface ($n_i=1.518$) thus producing spherical aberrations when focussing away from the coverslip. In the second case, we perfectly matched the sample ($n_i=1.518$) with the glass-oil-interface ($n_i=1.518$), thus minimizing spherical aberrations.

3.1.1 Resolution improvement by deconvolution

Firstly, we determined the resolution of the confocal microscope before and after deconvolution of confocal data of beads in the n_i -mismatched and n_i -matched case with the detector pinhole set at 1 Airy Unit (AU). The resolution of the optical system taken from the raw images was $225 \text{ nm} \pm 12 \text{ nm}$ in x,y and $546 \text{ nm} \pm 18 \text{ nm}$ in z -direction in AF1-medium and $223 \text{ nm} \pm 11 \text{ nm}$ in x,y and $550 \text{ nm} \pm 19 \text{ nm}$ in z -direction in AF1+-medium (Fig.1A, table 1). After deconvolution, we observed a 1.7-fold increase in lateral resolution for both mounting media, a 2.8-fold increase in axial resolution for AF1 and a 2.5-fold increase for AF1+ for beads imaged next to the coverslip (Fig. 1 A, table 1). The resolution values for AF1 and AF1+-mounted beads were comparable, corroborating previous findings, that close to the coverslip, a refractive index mismatch does not impair lateral and axial resolution since high numerical aperture objectives are corrected for this [13, 18]. Having established that deconvolution improves indeed the resolution of confocal data, we secondly analysed how the refractive index mismatch would impact resolution when looking at beads at a depth of $60 \mu\text{m}$ (Fig 1B, deconvoluted data, table 1). The lateral resolution of the beads was comparable for the two mounting media, which confirmed that the lateral resolution in depth is not impaired in a mismatched system [12, 17]. However, axial resolution was 2.2-times inferior in AF1-medium compared to AF1+-medium. Besides, we observed a considerable loss of peak intensity at a depth of $60 \mu\text{m}$ in AF1-medium. We had to adjust the laser power accordingly in order to exploit the full dynamic range of the image. This confirms the data, we published recently for beads measured in CFM3, another high refractive index mounting medium ($n_i=1.518$) where we observed the same phenomenon [17]. The axial resolution of beads remained constant in depth compared to the coverslip when applying refractive index matching with AF1+. This means that spherical aberration is minimized when using AF1+ medium, and our observation corroborated previous theoretical and experimental findings of Hell and co-workers [12] and our own findings for a perfectly matched system [17].

3.1.2 Resolution improvement by closing the pinhole aperture

We then wanted to test if we could increase resolution of the confocal microscope by closing the detection pinhole. We compared resolution at the coverslip and in a depth of 60 μm with the detector pinhole set to 0.6 AU (Fig. 1C, table 1) and after deconvolution of the data. Our choice of the 0.6 AU pinhole size was based on several tests on our biological data. We acquired the same type of biological sample with different pinhole sizes, from 1 AU to 0.4 AU and observed that 0.6 AU is the threshold where we discard enough diffraction signal without photo-bleaching and with a good contrast. Since the result depends largely on the quality and the photo-stability of the biological sample the optimal pinhole value has to be evaluated for each biological sample.

We observed lateral resolutions of $120 \text{ nm} \pm 5 \text{ nm}$ (coverslip) and $136 \text{ nm} \pm 9 \text{ nm}$ (depth) and axial resolutions of $182 \text{ nm} \pm 10 \text{ nm}$ (coverslip) and $471 \text{ nm} \pm 89 \text{ nm}$ (depth) for the AF1 medium (Fig. 1C, table 1). We had again to compensate for the loss of peak intensity by adjusting the laser power with the AF1 medium as described before. For the AF1+-medium, lateral resolutions of $106 \text{ nm} \pm 4 \text{ nm}$ (coverslip) and $120 \text{ nm} \pm 7 \text{ nm}$ (depth) and axial resolutions of $164 \text{ nm} \pm 8 \text{ nm}$ (coverslip) and $192 \text{ nm} \pm 17 \text{ nm}$ (depth) were measured.

Fig. 1D and E show the direct comparison of the optical resolution at 1 AU and 0.6 AU close to the coverslip (Fig.1D, table 1) and in 60 μm depth (Fig.1E, table 1), respectively. We observed a 1.3-fold increase in lateral and axial resolution measured in AF1-medium close to the coverslip (Fig. 1D, table 1) when setting the detection pinhole to 0.6 AU. The use of AF1+ medium improved resolution 1.3-fold laterally and 1.4-fold axially at AU 0.6 at the coverslip (Fig1. D, table 1). In depth, a significant lateral and axial resolution improvement was observed only for AF1+-medium at 0.6 AU. Besides, the use of AF1+ allowed maintaining a good axial resolution of $192 \text{ nm} \pm 17 \text{ nm}$ that is 2.5-times superior than with AF1-medium ($471 \text{ nm} \pm 89 \text{ nm}$), when closing the pinhole. It is thus advantageous to use refractive index matching when closing the detector aperture and imaging in depth.

Closing the pinhole indeed increased lateral and axial resolution 1.3 to 1.4-fold. These results are in good agreement with data measured by Cox and Sheppard [28], who observed a 1.4-fold increase in resolution after closing the pinhole aperture to 0.5 using a Leica TSC SP2 confocal microscope.

By optimizing sample preparation, image acquisition parameters and performing deconvolution, our workflow allowed us to obtain a considerable gain in lateral and axial resolution throughout the sample thickness. Firstly, the lateral resolution attained with 100 nm sub resolution fluorescent beads close to the coverslip attained a value of $106 \text{ nm} \pm 4 \text{ nm}$. This is close to the real size of the beads and comparable to the values published earlier for 3D-SIM-imaging [4]. Secondly, the axial resolution we obtained with our workflow was $164 \text{ nm} \pm 8 \text{ nm}$ and is thus approximately 1.6-fold better than the values published for 3D-SIM by Gustafsson [4]. However, these results are in good agreement with a paper by Schrader and colleagues [29], who demonstrated earlier that a resolution of 80 nm could be obtained axially on 50 nm gold particles with a confocal microscope and after

deconvolution. Given that we used 100 nm beads, our results are consistent with these previous findings. Thirdly, refractive index matching of the sample allowed to maintain 3D-SIM-like resolution of $120 \text{ nm} \pm 7 \text{ nm}$ laterally and $192 \pm 17 \text{ nm}$ axially in a depth of $60 \mu\text{m}$. This depth surpasses by a factor 3 the imaging depth of standard 3D-SIM [6].

3.2 Deconvolution optimization in biological data

Having established optimal image acquisition parameters, we then wanted to apply our workflow on biological samples and chose the meiotic spindle of the mouse oocyte labelled with alpha-tubulin coupled with FITC. We acquired 3D-images of meiotic spindles with a pinhole size of 0.6 Airy units at a sampling rate of 40 nm in x,y and 83 nm in z-direction. We wanted to determine the optimal deconvolution parameters and tested the Classic Maximum Likelihood Estimation (CMLE) and the Good's roughness Maximum Likelihood Estimation algorithm (GMLE), implemented in Huygens deconvolution software. CMLE and GMLE are iterative restoration method optimizing the likelihood of an estimate of the object given the measured image and the PSF. We also studied the influence of denoising prior to deconvolution using the Pure Denoising plugin implemented in ImageJ [26, 27, 28]. Finally we compared raw data and data optimized by our workflow after 3D-reconstruction.

3.2.1 Establishment of the optimal Regularisation Parameter (R-parameter)

The Huygens software uses what the manufacturer calls the Signal-to-Noise ratio as a Regularization Parameter (R-parameter), i.e. as a parameter that controls the sharpness of the restoration result. We will employ the term R-parameter in the following in order to avoid confusion with the image intrinsic Signal-to-Noise ratio (SNR) that we calculated to evaluate image quality.

The R-parameter is calculated as the square root of the number of photons in the brightest part of the image and controls the sharpness of the restoration result. The higher the R-parameter, the sharper the deconvolution result. R-parameter values recommended by the manufacturer for noise-prone confocal data lie between 15 and 20. Since we used a low-level-noise detector for confocal imaging, we tested R-parameter values between 16 and 34. After adjusting the R-parameter, we visually inspected the deconvolution result and observed that at an R-parameter >26 , microtubules were separated optimally, when compared to the raw image (Fig. 2 A-D). We also carried out fluorescence intensity profile measurements to obtain a measurement of the separation of tubulin structures in a single plane (Fig. 2A'-D4) and calculated the image inherent SNR before and after deconvolution to estimate image improvement. We noticed that microtubule separation attained a maximum, setting the R-parameter to 30 (Fig. 2 A'-D'). The SNR increased from 3,1 in the raw image to 3,32 after deconvolution with R-parameter set to 26. We started separating 5 peaks in the region of interest at an R-parameter of 28 (Fig. 2C', box). At higher R-parameter, the SNR

decreased slightly to 3.24 (R-parameter 28) and 3.20 (R-parameter 30), showing that the R-parameter introduces sharpness into the image. When using R-parameters >30 we started introducing deconvolution artefacts such as patterning, indicating that an R-parameter of 30 is optimal for our dataset (Fig 1, Supplementary Data 1 A-C).

3.2.2 Influence of denoising on the deconvolution of confocal data

Having established the optimal R-parameter, we now aimed at studying the impact of denoising before deconvolution. It has been proposed that denoising may be crucial before deconvolution and may improve the restoration result [30]. We therefore denoised the confocal data with the “Pure Denoising” plugin implemented in ImageJ [25, 26, 27]. This plugin is well adapted for Poisson noise, which is characteristic of fluorescence images. It estimates automatically noise parameters such as detector gain, detector offset and the standard deviation of the additive white Gaussian noise. We adjusted the number of cycle-spins and the number of adjacent frames used to maximum values in order to get the highest quality for our images. Denoising with the quality criteria set to maximum was rather computing intense and took several hours for a 3D-image stack. Fig. 3 shows a comparison of the raw image (A, A'), the denoised image (B, B'), the deconvolution of the raw image (C, C') and the deconvolution of the denoised image (D, D'). When inspecting the fluorescence intensity profiles, denoising alone did not improve the resolution of the image (Fig. 3B, B'), even if it improved considerably the SNR. We observed a smoothing of the fluorescence intensity profile (Fig. 3B', box). We then compared the deconvoluted dataset (Fig. 3C, C', box) with the denoised and deconvoluted image (Fig. 3D, D', box). We observed 5 main peaks in the region of interest of the deconvoluted image (Fig. 3C'). Denoising improved SNR of the restoration result. After denoising we were still able to distinguish 5 peaks (Fig. 3D, D' and box), even if the indentation was less prominent than in the non-denoised dataset (Fig. 3C, C', box). The overall aspect of the image was smoother and as a result microtubules appeared less spotty after denoising (Fig. 3 D, insert).

3.2.3 Comparison of CMLE and GMLE algorithm for the deconvolution of confocal data

In a last step, we wanted to compare the CMLE-algorithm with the Goods Maximum Likelihood Estimation (GMLE) algorithm. The GMLE-methods needs 4-times less iterations than the CMLE-method to obtain comparable restoration results, thus saving computation time. We compared the image after deconvolution with the CMLE-algorithm (Fig. 4A, A') with that deconvoluted with the GMLE-algorithm (Fig. 4B, B'). After visual inspection, we observed that the GMLE-algorithm smoothed the deconvolution result more than the CMLE-algorithm. Both algorithms gave comparable results in separating the microtubules and 5 main peaks could be distinguished in both cases (Fig. 4A', B', box), however, the SNR was higher for the GMLE-algorithm. Denoising did improve the SNR

of the image deconvoluted with CMLE-algorithm, however, the SNR after GMLE-deconvolution remained constant, indicating that denoising did not further improve image quality in this situation (Fig. 4, D, D').

3.2.4 Influence of refractive index matching on the 3D-image resolution

We have shown previously, that refractive index matching greatly improves axial resolution of confocal data in the mouse brain [17]. We therefore mounted mouse oocytes in AF1 and AF1+, respectively and performed 3D imaging. Fig. 5 shows lateral and axial views of the tubulin staining and after deconvolution. We observed a 2-fold increase of lateral resolution when comparing raw data to deconvoluted data. When considering the lateral maximum projection, the overall aspect of the image in the two mounting media was comparable (Fig. 5 A, B). We then measured the diameter of microtubule bundles throughout the depth of the image stacks and detected comparable lateral resolution for AF1 and AF1+ (Fig. 5 A, A'). However, axial resolution seemed to be better in the ri-matched sample with AF1+ after visual inspection (Fig. 5 B'). We measured axial resolutions and found indeed a 1.4-fold increase of resolution in AF1+-medium, meaning that refractive index matching is crucial in the biological sample. This confirms the data obtained with beads, where a comparable gain of axial resolution has been observed in depth using the ri-matched system (Fig. 1C) and our data on biological samples published earlier [17].

3.3 3D-reconstruction of the meiotic spindle

Having established all optimal parameters, we applied them to acquire 3D-stacks of triple stained mouse oocytes. We evaluated the overall aspect of the meiotic spindle resolution. We used alpha-tubulin coupled to FITC, to mark microtubules, Crest, a protein staining the kinetochore, which was revealed with a secondary antibody coupled to Cy3, and Hoechst to stain the chromosomes. Fig. 6 shows the 3D rendering of the raw data (A) and the deconvoluted data (B) of the meiotic spindle. We observed a clear improvement in resolution and much better separated microtubules (Fig. 6 B', arrows) and the kinetochores (Fig. 6 B', arrowheads) as compared to the raw data (Fig. 6 A', arrows and arrowheads). With these results, we provide evidence that our workflow, consisting of refractive index matching, optimized image acquisition and deconvolution improves greatly the overall resolution of the meiotic spindle image.

4. Conclusion

The proposed workflow provides an important benefit to confocal imaging of fixed samples with a high numerical aperture lens. We show first with beads that deconvolution improves by 1.7-fold lateral and by >2.6-fold the axial resolution of confocal data. Secondly, we provide evidence that

refractive index matching is particularly important to improve resolution and signal strength of the confocal system, when imaging in depth, where we obtain a 2.2-fold axial resolution improvement for the matched system. Thirdly, we show that closing the pinhole improves lateral and axial resolution by a factor 1.3 close to the coverslip and that the spatial invariance of the PSF in depth is crucial to preserve resolution in depth. We observe that deconvolution of the biological confocal data improves 2-fold the resolution compared to raw confocal data and that refractive index matching helps to maintain optimal axial resolution in the biological sample. We lastly show that denoising is advantageous for image quality when using the CMLE-algorithm, however, it is time consuming. Denoising is not necessary when using the GLME-algorithm, which also needs much less computing time. Summarized from these results, we were able to obtain confocal images having a 3D-SIM-like resolution in a rather bulky sample, the mouse oocyte. It would be of further interest to apply our workflow on other biological samples and see if we are able to maintain a 3D-SIM-like resolution at the full working distance of the objective (140 μm).

5. Acknowledgements

The authors thank Jean-François Gilles and Nicolas Heck for helpful discussions and Marc Dos Santos for precious help with statistical analysis and Adobe Illustrator. Work on mouse oocytes was supported by an ANR Grant (ANR-12-BSV2-0005-01) to KW. Confocal work was carried out at the Institute of Biology Paris-Seine Imaging Facility that is significantly (or: which receives significant support from...) supported by the "Conseil Regional Ile-de France", the French national research council (CNRS) and Sorbonne University, UPMC Univ Paris 06.

Figure legends:

Fig. 1: Resolution measurements with sub-resolution microspheres: influence of deconvolution, refractive index and pinhole aperture

100 nm green fluorescent beads were used to measure the lateral and axial resolution of the optical system at the coverslip and in 60 μm depth. For excitation, the 488 nm laser line was used and two series with the detection pinhole set to 1 Airy Unit (AU) and 0.6 AU were acquired. The Full Width at Half Maximum (FWHM) was measured using a line profile in x, y-direction and x, z-direction in the maximum intensity plane of the image stack, respectively and transferred to a graph (A-E). All data in brackets are given as mean \pm SD and have the unit nm.

(A) Raw bead images (black and dotted bars) and deconvoluted bead images (striped and white bars) taken at the coverslip were compared. Deconvolution improved significantly the lateral (raw: 225 ± 12 ; decon: 134 ± 3) and axial resolution (raw: 546 ± 18 ; decon: 193 ± 13) of beads in AF1.

Deconvolution improved also significantly the lateral (raw: 223 ± 11 ; decon: 134 ± 3) and axial resolution (raw: 550 ± 19 ; decon: 224 ± 18) of beads in AF1+-medium.

(B, C) Lateral and axial resolution of deconvoluted bead images at the coverslip (black and dotted bars) and in 60 μm depth (striped and white bars) at 1 AU (B) and 0.6 AU (C). Resolution measurements in depth show a significant axial resolution loss in AF1-medium at 1 AU (coverslip: 193 ± 13 ; depth: 453 ± 89) and at 0.6 AU (coverslip: 182 ± 10 ; depth: 471 ± 89).

(D, E) Comparison of the resolution of beads taken at 1 Airy unit (black and dotted bars) and 0.6 Airy unit (striped and white bars) at the coverslip (D) and in 60 μm depth (E). Resolution measurements at the coverslip (D) show a significant lateral resolution improvement when closing the pinhole to 0,6 AU in AF1-medium (1 AU: 134 ± 3 ; 0.6 AU: 120 ± 5 , Mann-Whitey test, $p= 0.0001$), and a substantial axial resolution increase (1 AU: 193 ± 13 ; 0.6 AU: 182 ± 10 , Mann-Whitey test, $p= 0.0001$). A significant lateral resolution improvement at 0.6 AU is also observed in AF1+-medium (1 AU: 134 ± 3 ; 0.6 AU: 106 ± 4 , Mann-Whitey test, $p= 0.0001$) and axial resolution improves substantially, too (1 AU: 210 ± 21 ; 0.6 AU: 192 ± 17 , Mann-Whitey test, $p= 0.0001$).

In depth (E), no resolution improvement is observed laterally (1 AU: 140 ± 10 ; 0.6 AU: 136 ± 9) or axially (1 AU: 453 ± 89 ; 0.6 AU: 471 ± 89) in AF1-medium. However, when using AF1+-medium, resolution improves significantly in the lateral direction (1 AU: 133 ± 6 ; 0.6 AU: 120 ± 7 , Mann-Whitey test, $p= 0.0001$) and in the axial direction (1 AU: 210 ± 21 ; 0.6 AU: 192 ± 17 , Mann-Whitey test, $p= 0.0003$).

Fig. 2: Determination of optimal deconvolution parameters, R-Parameter

Mouse oocytes stained with FITC-tubulin and imaged at 488 nm with the detection pinhole adjusted to 0.6 Airy Unit and taken with a 40 nm pixel size and an 83 nm z step size were deconvoluted varying the R-parameter between 26, 28 and 30. Images show x, y-maximum projections of the raw data (A), and the deconvoluted data with R-parameter 26 (B), R-parameter 28 (C), and R-parameter 30 (D). Inserts show the position of the line profile used for fluorescence intensity measurements shown in the graphs next to each image (A'-D'). S/N-ratios indicated in (A'-D') are a value for the image intrinsic noise and were calculated as described in (2.8). The boxes indicate the regions of interest, where 5 main peaks can be separated after deconvolution. Note that R-parameter of 30 gave best results. Scale bar is 5 μm .

Fig. 3: Influence of denoising on the deconvolution result

Images show x, y-maximum projections of the raw data (A), the deconvoluted data (B), the denoised data (C) and the denoised, deconvoluted data (D). Deconvolution was carried using the CMLE-algorithm (R-parameter=30, 500 iterations). Inserts show the position of the line profile used for

fluorescence intensity measurements shown in the graphs next to each image (A'-D'). S/N-ratios are indicated in (A'-D'). The boxes indicate the regions of interest, where 5 main peaks can be separated after deconvolution. Note that denoising considerably improves the S/N-value of the raw data. Deconvoluted data and a combination of denoising and deconvolution gave comparable results. However, denoising improves the S/N-value of the deconvoluted data. Scale bar is 5 μm .

Fig. 4: Comparison of deconvolution algorithm CMLE and GMLE

Images show data deconvoluted with two different deconvolution algorithms implemented in the Huygens software, the Classical Maximum Likelihood Estimation (CMLE) and the Good's Maximum Likelihood Estimation (GMLE). Deconvolution was carried with the R-parameter set to 30 for both methods. Images show x, y-maximum projections of the CMLE-deconvoluted data (A), the GMLE deconvoluted data (B) the denoised, CMLE deconvoluted data (C), and the denoised, GMLE deconvoluted data (D). Inserts show the position of the line profile used for fluorescence intensity measurements shown in the graphs next to each image (A'-D'), the boxes indicate the position of the 5 main peaks compared before. Note that denoising improves the S/N of the CMLE-method, but not of the GMLE-method. The GMLE-algorithm gives the best visual result. Scale bar is 5 μm .

Fig. 5: Impact of refractive index matching in mouse oocytes

Images show x, y-maximum projections (A, B, lateral view), a cut-out of a single plane in a depth of 10 μm (insert of A, B) and x, z-projections (A', B') of mouse oocytes stained with FITC-tubulin and imaged at 488 nm in AF1-medium (A, A') and AF1+-medium (B, B'). All data in brackets are given as mean \pm SD and have the unit nm.

Microtubule bundle diameters were measured in single images of raw data (images not shown) and deconvoluted data (raw data/ deconvoluted data; 390 ± 131 / 218 ± 45). A 2-fold amelioration of resolution was noted after deconvolution. Lateral resolution of microtubule bundles in AF1 and AF1+-medium was comparable (AF1/ AF1+; 232 ± 33 / 204 ± 57). Axial resolution of microtubule bundles was measured in AF1 and AF1+-medium (AF1/ AF1+; 402 ± 107 / 292 ± 49). Note that refractive index matching with AF1+ improves considerably the axial resolution (A', B'). Scale bars are 5 μm .

Fig. 6: 3D-reconstruction of data

Mouse oocytes were triple stained with Hoechst (chromosomes), FITC (microtubules) and CY3 (kinetochores). Images show 3D-renderings of raw data (A- A') and deconvoluted data (B-B'). Magnifications of a region of (A, B) with arrows indicating microtubules (A', B') and arrowheads

showing kinetochores (A', B') show the resolution improvement after deconvolution, where separate microtubules and two adjacent kinetochores can clearly be separated.

Supplementary data 1:

Images show data deconvoluted with two different deconvolution algorithms implemented in the Huygens software, the Classical Maximum Likelihood Estimation (CMLE) and the Good's Maximum Likelihood Estimation (GMLE). Deconvolution was carried with the R-parameter set to 30, 32 and 34 for both methods. Images show x, y-maximum projections of the CMLE-deconvoluted data (A) and the GMLE deconvoluted data (B). Inserts show magnifications of microtubules. R-parameters >30 improve the S/N of the GMLE-method, but not of the CMLE-method. When using R-parameters >30 we started introducing deconvolution artefacts such as patterning when using the CMLE-method (inserts), indicating that an R-parameter of 30 is optimal for our dataset. Scale bar is 5 μm .

Supplementary data 2: Influence of immersion oil refractive index on axial resolution of sub-resolution fluorescent beads. Note that axial resolution is best with immersion oil harbouring refractive index of 1.516-1.518.

Supplementary data 3: Determination of bead resolution (A) and xz view of beads (B) comparing their PSF when images at the coverslip and at depth in both non-matched (AF1) and matched RI (AF1+).

Supplementary data 4: To calculate the SNR, images were thresholded with the Shanbhag mode on ImageJ. We create a mask from the duplicated image. Two selections are necessary: one for measuring the average intensity of the signal, the other for measuring the background. We finally calculate the SNR as average intensity signal/average intensity background.

References

- [1] L. Schermelleh, R. Heintzmann, H. Leonhardt, A guide to super-resolution fluorescence microscopy. *J. Cell. Biol.* 26; 190 (2) (2010) 165-75.
- [2] M. G. Gustafsson, Surpassing the lateral resolution limit by a factor of two using structured illumination microscopy. *J. Microsc.* 198 (Pt 2) (2000) 82-7.
- [3] R. S. Fischer, Y. Wu, P. Kanchanawong, H. Shroff, C. M. Waterman, Microscopy in 3D: a biologist's toolbox. *Trends Cell. Biol.* 21(12) (2010) 682-91.

- [4] M. G. Gustafsson, L. Shao, P. M. Carlton, C. J. Wang, I. N. Golubovskaya, W. Z. Cande, D. A. Agard, J. W. Sedat, Three-dimensional resolution doubling in wide-field fluorescence microscopy by structured illumination. *Biophys. J.* 94(12) (2008) 4957-70.
- [5] P. W. Winter, A. G. York, D. D. Nogare, M. Ingaramo, R. Christensen, A. Chitnis, G. H. Patterson, H. Shroff, Two-photon instant structured illumination microscopy improves the depth penetration of super-resolution imaging in thick scattering samples. *Optica.* 20; 1(3) (2014) 181-191.
- [6] K. Nienhaus, G.U. Nienhaus, Where Do We Stand with Super-Resolution Optical Microscopy? *J. Mol. Biol.* 29; 428 (2 Pt A) (2016) 308-22.
- [7] A. G. York, S. H. Parekh, D. Dalle Nogare, R. S. Fischer, K. Temprine, M. Mione, A. B. Chitnis, C. A. Combs, H. Shroff, Resolution doubling in live, multicellular organisms via multifocal structured illumination microscopy. *Nat. Methods* 13;9(7) (2012) 749-54.
- [8] J. B. Pawley, Fundamental Limits of Confocal Microscopy, *Handbook of Biological Confocal Microscopy*, third edition, Springer, New York, Chapter 2, Pages 20-42
- [9] M. B. Cannell, A. McMorland, and C. Soeller, Image enhancement by deconvolution, *Handbook of Biological Confocal Microscopy*, third edition, Springer, New York, Chapter 25, (2006) Pages 488-500
- [10] Shaw P. J, Comparison of widefield/deconvolution and Confocal microscopy for Three-Dimensional Imaging. *Handbook of Biological Confocal Microscopy*, third edition, Springer, New York, Chapter 23, (2006) 453-467
- [11] N. Heck, S. Betuing, P. Vanhoutte, J. Caboche, A deconvolution method to improve automated 3D-analysis of dendritic spines: application to a mouse model of Huntington's disease. *Brain Struct. Funct.* 217 (2) (2012) 421-34.
- [12] A. Egner, and S. W. Hell, Aberrations in confocal and Multi-photon Fluorescence Microscopy induced by refractive index mismatch. *Handbook of Biological Confocal Microscopy*, third edition, Springer, New York, (2006) 404-412
- [13] M. Von Tiedemann, A. Fridberger, M. Ulfendahl, I. Tomo, J. Boutet de Monvel, Image adaptive point-spread function estimation and deconvolution for in vivo confocal microscopy. *Microsc. Res. Tech.* 69(1) (2006) 10-20
- [14] A. Dieterlen, C. Xu, M.-P. Gramain, O. Haeberlé, B. Colicchio, C. Cudel, S. Jacquy, E. Ginglinger, G. Jung, E. Jeandidier, Validation of image processing tools for 3-D fluorescence microscopy. *Comptes Rendus Biologies*, Elsevier Masson, 325 (1) (2002) 327-334.
- [15] M. Booth, D. Andrade, D. Burke, B. Patton, M. Zurauskas, Aberrations and adaptive optics in super-resolution microscopy. *Microscopy (Oxf).* 64(4) (2015) 251-61.
- [16] T. Staudt, M. C. Lang, R. Medda, J. Engelhardt, S. W. Hell, 2,2'-thiodiethanol: a new water-soluble mounting medium for high-resolution optical microscopy. *Microsc. Res. Tech.* 70 (1) (2007) 1-9.

- [17] C. Fouquet, J.-F. Gilles, N. Heck, M. Dos Santos, R. Schwartzmann, V. Cannaya, M.-P. Morel, R. S. Davidson, A. Trembleau, S. Bolte, *Plos One* (2015): DOI: 10.1371/journal.pone.0121096
- [18] M.W. Kirschner, T. Mitchison, Microtubule dynamics, *Nature* 324 (1986) 621.
- [19] R. Alfaro-Aco, S. Petry, Building the Microtubule Cytoskeleton Piece by Piece, *J. Biol. Chem.* 290 (28) (2015) 17154-62.
- [20] S. A. Touati, E. Buffin, D. Cladière, K. Hached, C. Rachez, J. M. van Deursen, K. Wassmann, Mouse oocytes depend on BubR1 for proper chromosome segregation but not for prophase I arrest, *Nat Commun.* (2015) 21; 6: 6946
- [21] J. P. Chambon, K. Hached, K. Wassmann, Chromosome spreads with centromere staining in mouse oocytes, *Methods Mol Biol.* (2013) 957:203-12.
- [22] K. Hached, S. Z. Xie, E. Buffin, D. Cladière, C. Rachez, M. Sacras, P. K. Sorger, K. Wassmann, Mps1 at kinetochores is essential for female mouse meiosis I, *Development* (2011) 138(11):2261-71.
- [23] W.S. Rasband, ImageJ, US National Institutes of Health, Bethesda, MD, U.S.A. <http://rsb.info.nih.gov/ij/>((1997–2016), (accessed 2016).
- [24] F. de Chaumont, S. Dallongeville, N. Chenouard, N. Hervé, S. Pop, T. Provoost, V. Meas-Yedid, P. Pankajakshan, T. Lecomte, Y. Le Montagner, T. Lagache, A. Dufour, J. C.Olivo-Marin, Icy: an open bioimage informatics platform for extended reproducible research. *Nat Methods.* 28; 9(7) (2012) 690-6
- [25] F. Luisier, C. Vonesch, T. Blu, M. Unser, "Fast Interscale Wavelet Denoising of Poisson-corrupted Images", *Signal Processing*, vol. 90, no. 2, (2010) 415-427,.
- [26] F. Luisier, "The SURE-LET Approach to Image Denoising", *Swiss Federal Institute of Technology Lausanne, EPFL Thesis no. 4566* (2010), 232
- [27] F. Luisier, C. Vonesch, T. Blu, M. Unser, "Fast Haar-Wavelet Denoising of Multidimensional Fluorescence Microscopy Data", *Proceedings of the Sixth IEEE International Symposium on Biomedical Imaging: From Nano to Macro (ISBI'09, Boston MA, USA, June 28-July 1, 2009*, pp. 310-313.
- [28] G. Cox, C. J. Sheppard, Practical limits of resolution in confocal and non-linear microscopy. *Microsc Res Tech.* 1; 63 (1) (2004) 18-22.
- [29] M. Schrader, S. W. Hell, H.T.M. Van der Voort, Potential of confocal microscopes to resolve in the 50-100 nm range, *Appl. Phys. Lett.* 69 (24) (1996) 3644-3646.
- [30] J. Boutet de Monvel, S. Le Calvez, M. Ulfendahl, Image restoration for confocal microscopy: improving the limits of deconvolution, with application to the visualization of the mammalian hearing organ, *Biophys. J.* 80 (5) (2001) 2455-70.

Figure 1

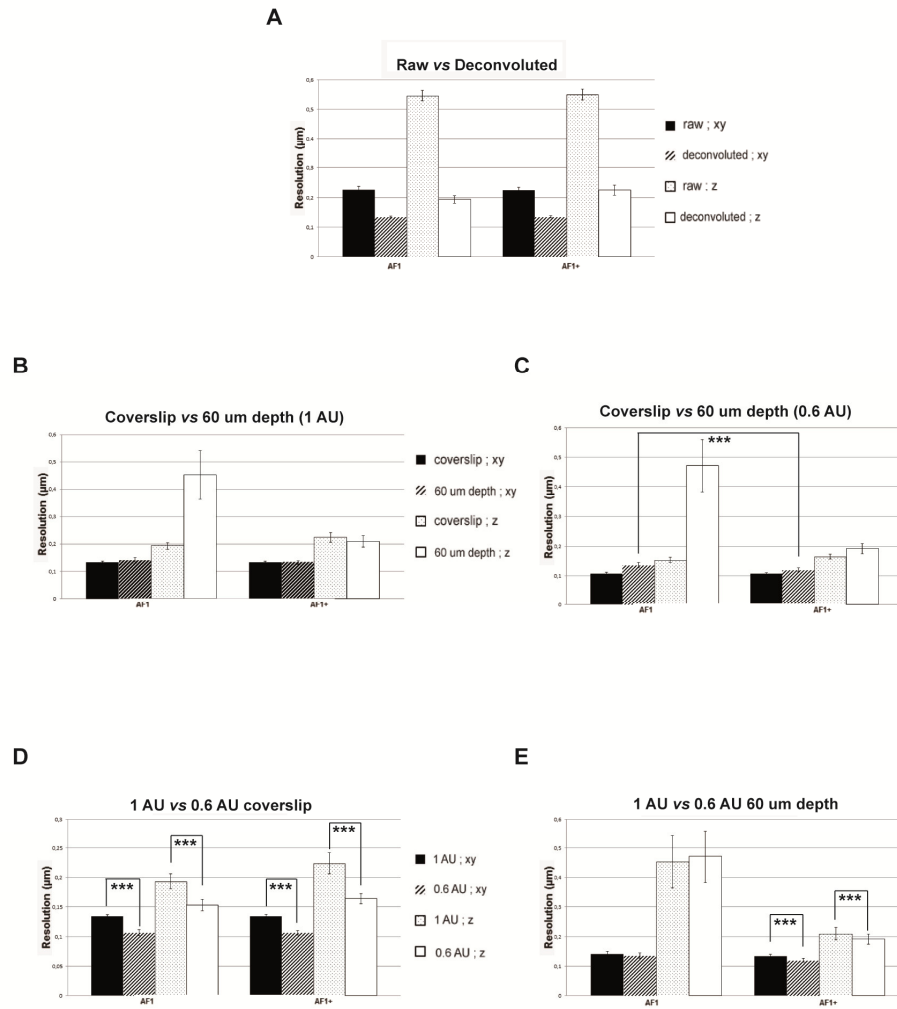


Figure 2

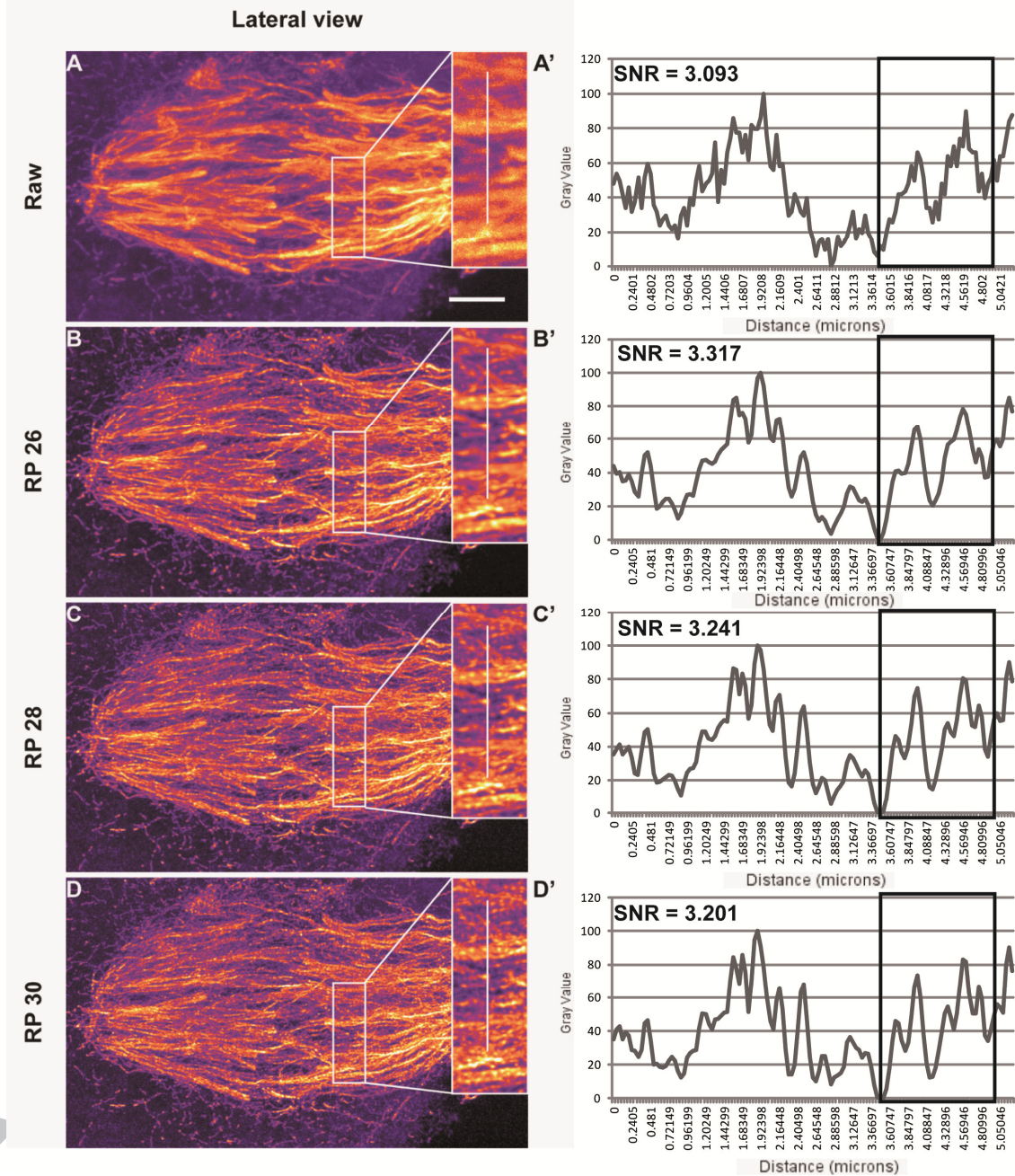


Figure 3

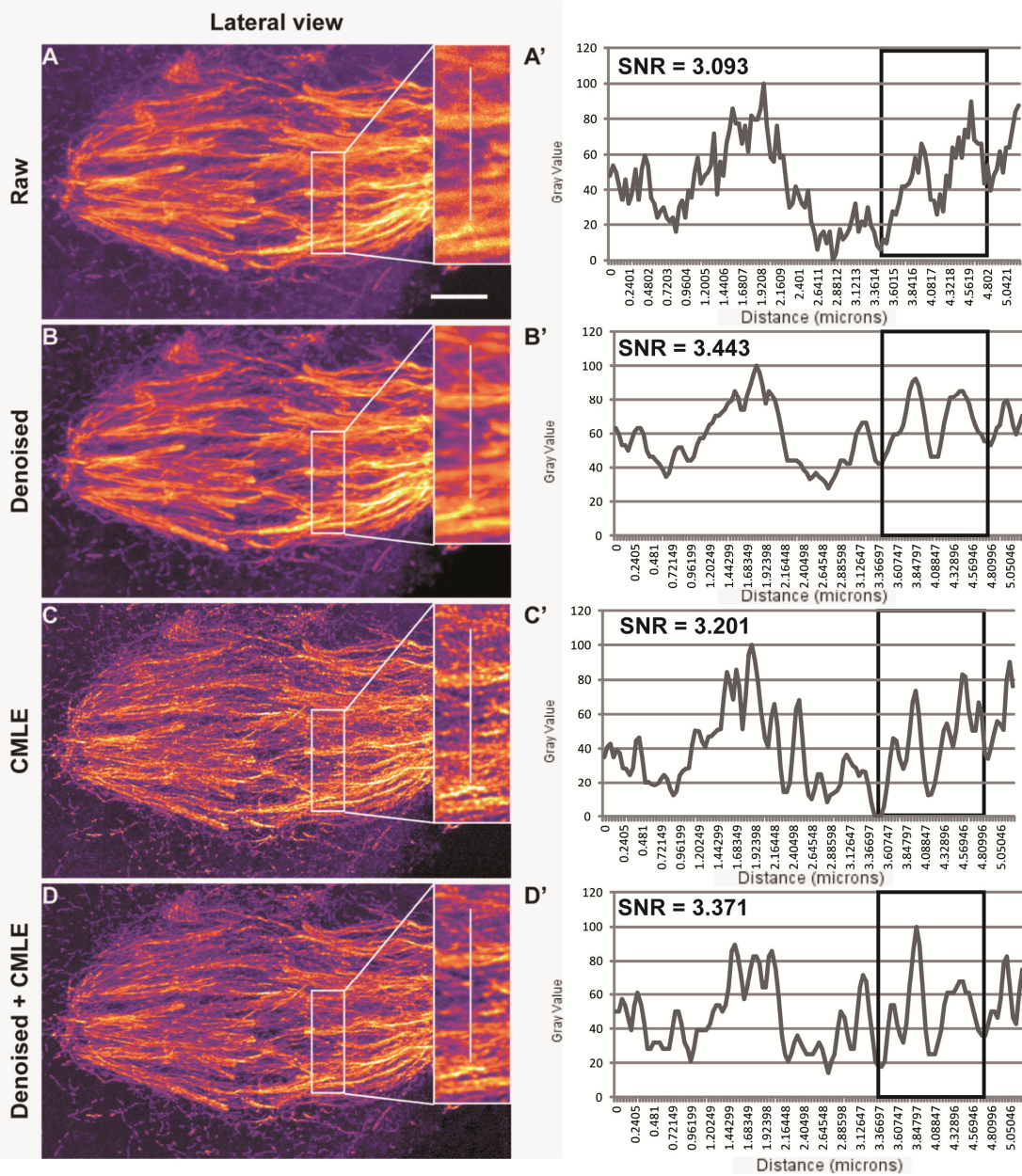


Figure 4

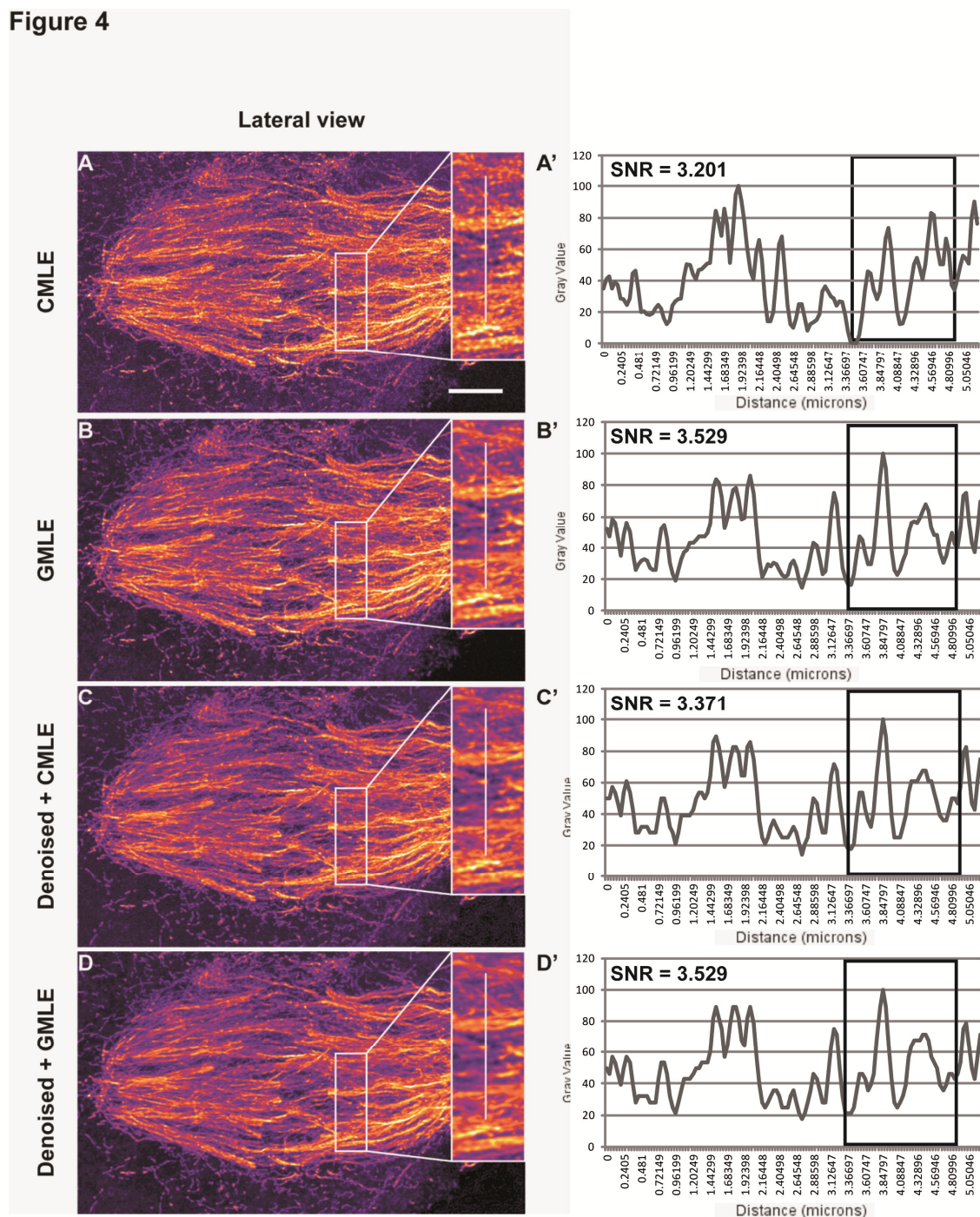


Figure 5

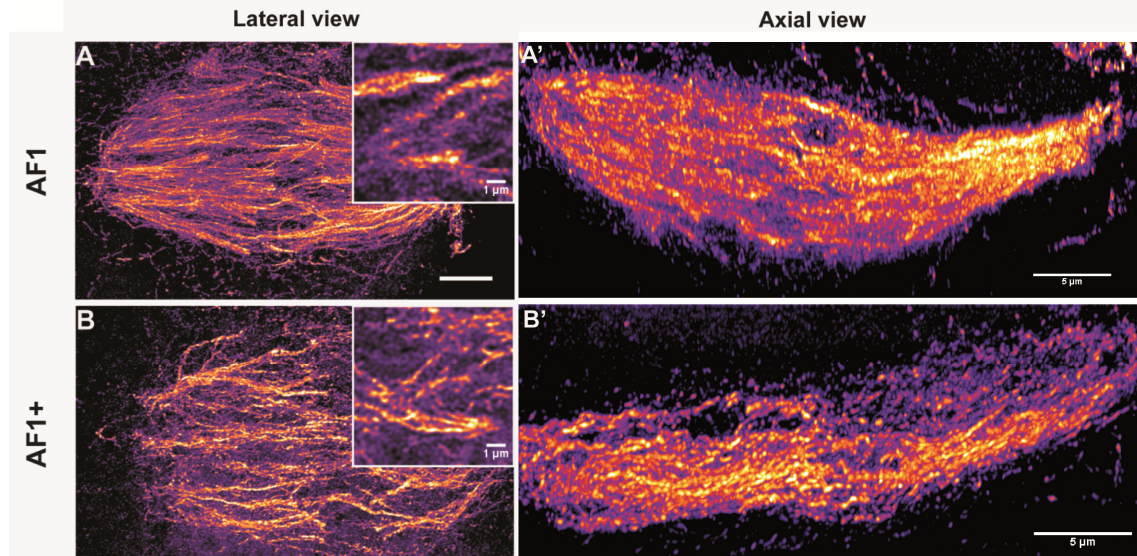
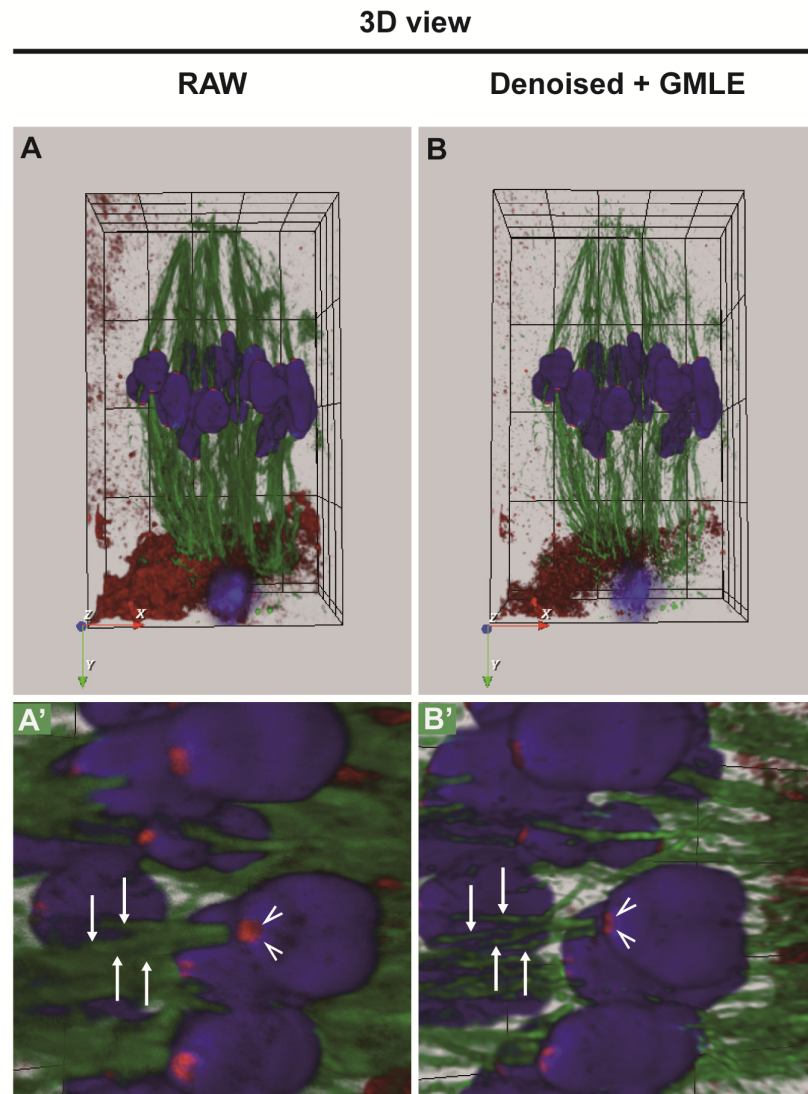


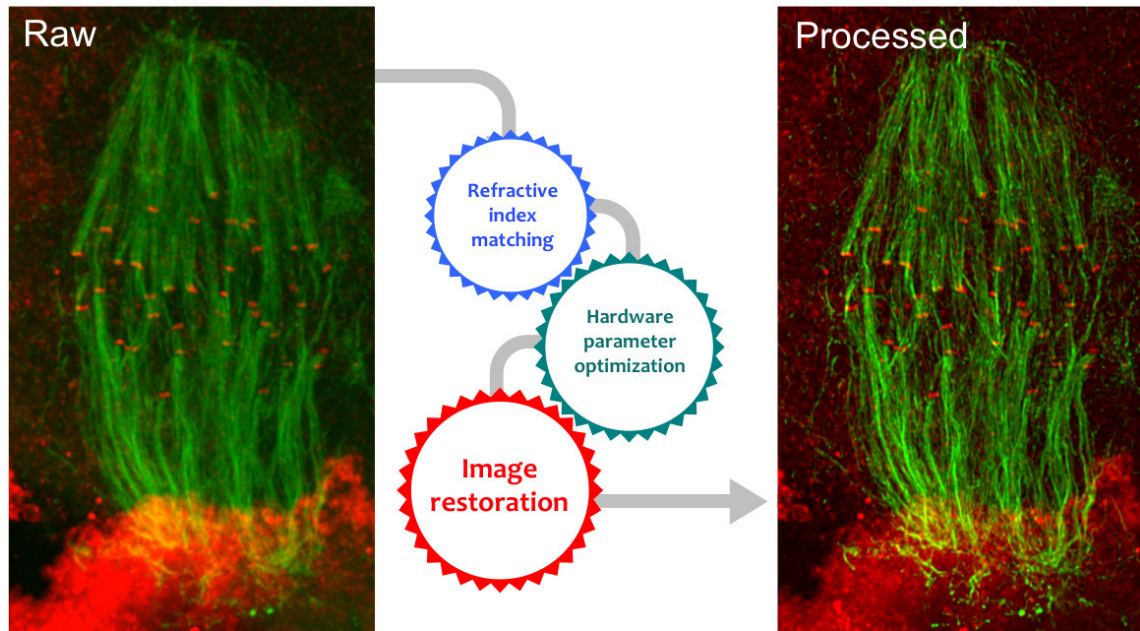
Figure 6



	AF1 coverslip		AF 60 μ m depth		AF1+ coverslip		AF1+ 60 μ m depth	
	1 AU	0,6 AU	1 AU	0,6 AU	1 AU	0,6 AU	1 AU	0,6 AU
xy (raw)	207 nm	177 nm	309 nm	294 nm	223 nm	182 nm	214 nm	203 nm
xy (deconvoluted)	121 nm	105 nm	140 nm	136 nm	134 nm	106 nm	133 nm	120 nm
z (raw)	416 nm	386 nm	1532 nm	1383 nm	550 nm	436 nm	509 nm	467 nm
z (deconvoluted)	167 nm	151 nm	453 nm	470 nm	224 nm	164 nm	210 nm	192 nm

Table 1 : Resolution measurement with fluorescent subresolution beads

Super-resolution for everybody: An image processing workflow to obtain high-resolution images with a standard confocal microscope, F. Lam, D. Cladière, C. Guillaume, K. Wassmann, and S. Bolte.



ACCEPTED MA